

**1 Focal mechanisms and size distribution of earthquakes
2 beneath the Krafla central volcano, NE Iceland**

Juerg Schuler,¹ David J. Pugh,^{2,3} Egill Hauksson,¹ Robert S. White,² Joann

M. Stock,¹ Bryndís Brandsdóttir,⁴

¹Seismological Laboratory, California
Institute of Technology, Pasadena, CA
91125, USA

²Bullard Laboratories, University of
Cambridge, Cambridge, CB3 0EZ, UK

³now at McLaren Applied Technologies,
Woking, UK

⁴Science Institute, University of Iceland,
Reykjavík, Iceland

3 **Abstract.** Seismicity was monitored beneath the Krafla central volcano,
4 NE Iceland, between 2009 and 2012 during a period of volcanic quiescence,
5 when most earthquakes occurred within the shallow geothermal field. The high-
6 est concentration of earthquakes is located close to the rock-melt transition
7 zone as the IDDP-1 wellbore suggests, and decays quickly at greater depths.
8 We recorded multiple swarms of microearthquakes, which coincide often with
9 periods of changes in geothermal field operations, and found that about one
10 third of the total number of earthquakes are repeating events. The event size
11 distribution, evaluated within the central caldera, indicates average crustal
12 values with $b = 0.79 \pm 0.04$. No significant spatial b -value contrasts are re-
13 solved within the geothermal field nor in the vicinity of the drilled melt. Be-
14 sides the seismicity analysis, focal mechanisms are calculated for 342 events.
15 Most of these short-period events have source radiation patterns consistent
16 with double-couple (DC) mechanisms. A few events are attributed to non-
17 shear faulting mechanisms with geothermal fluids likely playing an impor-
18 tant role in their source processes. Diverse faulting styles are inferred from
19 DC events, but normal faulting prevails in the central caldera. The best-fitting
20 compressional and tensional axes of DC mechanisms are interpreted in terms
21 of the principal stress or deformation-rate orientations across the plate bound-
22 ary rift. Maximum compressive stress directions are near-vertically aligned
23 in different study volumes, as expected in an extensional tectonic setting.
24 Beneath the natural geothermal fields, the least compressive stress axis is
25 found to align with the regional spreading direction. In the main geother-

26 mal field both horizontal stresses appear to have similar magnitudes caus-
27 ing a diversity of focal mechanisms.

1. Introduction

28 The Mid-Atlantic ridge, crossing Iceland, is expressed by en échelon arranged volcanic
29 systems that commonly include a central volcano and fissure swarm [Sæmundsson, 1979].
30 Our focus is the Krafla volcanic system in NE Iceland (Figure 1) comprising a 5-8 km-wide
31 and 100 km-long fissure swarm trending approximately N10°E and transecting its 21 km
32 by 17 km-wide central volcano and caldera [Hjartardóttir et al., 2012]. Its volcano, esti-
33 mated to be 0.5-1.8 Myr old [Brandsdóttir et al., 1997], underwent 35 eruptions since the
34 last glacial period [Björnsson et al., 1979]. The *Krafla fires* is the last rifting episode and
35 occurred between 1974-1984. It included 20 rifting events and 9 basaltic fissure eruptions
36 [Einarsson, 1991; Buck et al., 2006].

37 Based on the wave propagation path of regional earthquakes, Brandsdóttir and Einarsson
38 [1979] inferred that magma was stored in shallow chambers and sporadically injected into
39 dikes along the fissure swarm. Seismicity ceased after the rifting episode and has been
40 mostly confined to two high-temperature geothermal systems [e.g., Arnott and Foulger,
41 1994a; Schuler et al., 2015], where faults and fissures facilitate the transfer of hot geother-
42 mal fluids to the surface. The Bjarnarflag-Námafjall field is located outside whereas the
43 Krafla-Leirhnjúkur field is located inside the caldera. Geothermal drilling started in 1974
44 and energy production started in 1977. Drill cuttings from boreholes helped to construct
45 local geological profiles of the eastern and southeastern caldera [Ármannsson et al., 1987].
46 At Hvíthólar (Inset B, Figure 1), lavas and hyaloclastites dominate the upper 1.5-1.6 km
47 of the rock sequence followed by intrusive rocks (gabbro). In the Leirbotnar-Suðurhlíðar
48 area, lavas and hyaloclastites are encountered to 1.0 km depth or 0.5 km below sea level

49 (bsl) overlying gabbroic rocks, whereas to the east of Suðurhlíðar, gabbroic intrusive rocks
50 are found at 1.2-1.3 km bsl (from here onwards, we refer to depth as depth below the sur-
51 face if not followed by the acronym bsl).

52 While drilling the IDDP-1 borehole in 2009, rhyolitic melt was encountered at 2104 m
53 depth (1551 m bsl). Its location is 0.5 km southwest of the 1724 AD explosion crater Víti.
54 The melt likely originated from partially molten and hydrothermally altered crust [*Elders*
55 *et al.*, 2011; *Zierenberg et al.*, 2012]. Above the melt pocket at 1482-1527 m depth bsl, the
56 most productive zone for fluid injections was located in felsic rock [*Mortensen et al.*, 2014;
57 *Friðleifsson et al.*, 2015]. Another well, KJ-39, retrieved quenched silicic glass southeast
58 of IDDP-1 at 2062 m depth bsl [*Mortensen et al.*, 2010], but chemical differences indicate
59 no direct link between the melt sources.

60 Rhyolitic domes and ridges near the caldera rim suggest that magma chambers existed in
61 the past beneath the volcano, because these rhyolites were likely generated at the sides of
62 an active magma chamber [*Jónasson* , 2007]. Whether the drilled melt in IDDP-1 is part
63 of a large magma chamber has not been fully determined. Seismic studies [e.g., *Einarsson*,
64 1978; *Brandsdóttir and Menke*, 1992; *Schuler et al.*, 2015] as well as joint magnetotelluric
65 and transient electromagnetic soundings [e.g., *Árnason et al.*, 2009] point towards the
66 presence of a larger heat source emanating from multiple shallow dikes, a larger melt
67 pocket cooling at shallow depth, and/or heat being supplied from a depth further below.
68 Seismic data were acquired initially to image the shallow magma chamber [*Schuler et al.*,
69 2015]. Here, we investigate the earthquake seismicity and source mechanisms close to
70 the melt-rock interface and in the overlying geothermal field to better understand the

71 processes involved. In addition, we examine the crustal stress state or deformation rate
72 at Krafla a quarter century after the last rifting episode.

2. Data

73 A seismic array comprising 27 Guralp 6TD/30s and one ESPCD/60s instruments, com-
74 plemented by 4 LE-3D/5s stations that were operated by the Icelandic Meteorological
75 Office (IMO), collected data during the period from August 2009 to July 2012. Station
76 distributions changed slightly over time, which entails that we study and compare only
77 consistent subsets of data without testing the effect of a network change. Typically, 25 seis-
78 mometers were recording earthquakes down to local magnitudes (ML) of about -1. Noise
79 levels appear to be fairly constant at each receiver over different time periods. We used
80 the Coalescence Microseismic Mapping [*Drew et al.*, 2013] method for initial detection and
81 localization of earthquakes. Arrival-time picks of events with high signal-to-noise ratio
82 (SNR) were manually refined. Hypocenter locations were taken from *Schuler et al.* [2015],
83 who determined them by a 3D tomographic inversion. Improved relative locations (Figure
84 1) are achieved by double-difference calculations [*Waldhauser and Ellsworth*, 2000] using
85 the 3D velocity model. Hypocenter location errors, estimated during the tomographic
86 inversion, are mostly less than 150 m. The peak frequencies of *P*-wave first arrivals are
87 typically about 10 ± 2 Hz in the central part of the caldera.

3. *b*-values in volcanic areas

88 The size distribution of earthquakes within a seismogenic volume and time period is
89 commonly described by the power-law [*Ishimoto and Iida*, 1939; *Gutenberg and Richter*,
90 1944] $\log N = a - bM$, with N being the cumulative earthquake number of events with

101 magnitudes $\geq M$, a being the productivity of the considered volume, and b is the relative
102 size distribution. Some factors affecting the b -value are material heterogeneity [Mogi,
103 1962], thermal gradient [Warren and Latham, 1970], and applied stress [Scholz, 1968;
104 Schorlemmer et al., 2005]. For tectonic regions, b averages to about 1.0 [Frohlich and
105 Davis, 1993]. In volcanic areas, high b -values ($b \geq 1.3$) are mostly resolved in small vol-
106 umes embedded in average ($b \leq 1.0$) crust [e.g., Wiemer and McNutt, 1997]. In particular,
107 elevated b -values are found close to magma chambers, where strong heterogeneities, ther-
108 mal gradients, high pore pressures, extensive fracture systems, and circulating geothermal
109 fluids are expected [Wiemer and Wyss, 2002]. Volcanic zones that exhibit elevated b -
110 values, collocated with inferred magma pockets, have been reported for both deeper (7-10
111 km) and shallower (3-4 km) depths [McNutt, 2005]. McNutt [2005] recognized that there
112 is often a characteristic temporal b -value sequence associated with volcanic intrusions and
113 eruptions. The first short-term b -value peak is attributed to high geothermal gradients

107 At the Krafla volcano, Ward et al. [1969] estimated a $b = 0.84 \pm 0.29$ and $b = 0.83 \pm 0.16$
108 using P - and S -wave amplitudes, respectively, in the central part of the caldera prior to
109 the Krafla fires in 1967. During the rifting episode in 1978, Einarsson and Brandsdóttir
110 [1980] obtained a high b -value of 1.7 ± 0.2 for an earthquake swarm recorded during a
111 dike injection north of Leirhnjúkur. The Mid-Atlantic Ridge is another place where high
112 b -values were estimated during swarm activities [Sykes, 1970]. At Krafla, Arnott and
113 Foulger [1994a] recorded no major swarm activity after the last eruptive rifting episode

ended, with most events interpreted as mainshocks. They calculated $b = 0.95 \pm 0.23$ at Leirhnjúkur, $b = 0.62 \pm 0.14$ at Bjarnarflag, $b = 1.25 \pm 0.30$ in the dike zone between Bjarnarflag and Leirhnjúkur, and $b = 0.77 \pm 0.10$ of the entire region. The elevated values in the dike zone were likely caused by shallow intrusions [Arnott and Foulger, 1994a]. We investigate the size distribution next to the known location of melt to see whether increased values are found.

3.1. b -value estimation

For calculating earthquake magnitudes, we employ a local magnitude determination [Bormann et al., 2013] and calibrate the formula against the South Iceland Lowland (SIL) magnitudes reported by IMO. We remove the instrument responses from the waveforms and convolve the displacement data with the response of a Wood-Anderson seismograph. The maximum peak-to-peak amplitudes were automatically determined. Station corrections are applied to account for site-specific effects. A multi-station approach further reduces source-specific effects (e.g., directivity). However, smaller events are recorded at fewer stations and therefore have less well-constrained magnitude estimates. Our magnitudes and errors represent the mean magnitudes and errors that are calculated from the three-component recordings at each station. Carefully determining the magnitude of completeness (M_c), the minimum magnitude at which the earthquake catalogue is complete, is required before b -values are estimated [Wiemer and Wyss, 2002]. We estimated M_c using the entire-magnitude-range method described by Woessner and Wiemer [2005] as well as the maximum curvature method. The maximum likelihood b -value [Tinti and Mulargia, 1987] is determined by

$$b = \frac{1}{\log(10)\Delta M} \log \left(1 + \frac{\Delta M}{\overline{M} - M_c} \right), \quad (1)$$

135 where \overline{M} is the sampling average of the magnitudes. The bin width is constant and was
 136 determined by our average magnitude error of 0.2. In estimating the confidence limits,
 137 we follow *Shi and Bolt* [1982]. We decided to temporally map b -values within periods
 138 of constant station distributions and spatially at discrete nodes (grid cells). We set the
 139 minimum number of events within a volume to estimate the b -value to 100 earthquakes,
 140 double the minimum number suggested by Schorlemmer et al. (2004).
 141 Earthquake swarms may bias b -value estimation [*Farell et al.*, 2009], because it is based
 142 on a Poissonian event distribution. Related earthquakes, like fore- and after-shocks, are
 143 removed prior to calculating the background b . A cumulative rate method was employed to
 144 identify earthquake swarms using similar parameterizations to those described by *Jacobs*
 145 *et al.* [2013]. The minimum event number of a potential earthquake swarm was set to four
 146 above the average event rate. A distance rule is applied where earthquakes with greater
 147 distance than 10 km from the mean event location of a potential swarm are rejected.
 148 Finally, a time rule ensures that different swarm sequences are separated by at least four
 149 days. Whether b -values changed significantly after removing them from the complete event
 150 catalogue was evaluated following *Akaike's* (1974) Information Criterion (AIC). The AIC
 151 score of both original and declustered catalogues having the same b -values is compared to
 152 the score where the catalogues lead to different b -values. After *Utsu* [1992],

$$\Delta\text{AIC} = -2(N_1 + N_2) \ln(N_1 + N_2) + 2N_1 \ln\left(N_1 + \frac{N_2 b_1}{b_2}\right) + 2N_2 \ln\left(N_2 + \frac{N_1 b_1}{b_1}\right) - 2. \quad (2)$$

153 N stands for the number of earthquakes in each group. The difference in b -values are not
154 considered significant if $\Delta\text{AIC} < 2$ [Utsu, 1999].

4. Seismic source mechanisms

155 When shear slip occurs on a buried fault, shear stress is released in the form of elastic
156 waves. The far-field properties of these waves (polarities, amplitudes) are then used in
157 estimating the source radiation pattern or mechanism. Double-couple (DC) radiation
158 patterns are the result of shear slip on planar faults, whereas more complex radiation
159 patterns are summarized as non-DC resulting from non-shear faulting. Involvement of
160 fluids, slip along curved faults, and fractal faulting are some possible causes that lead to
161 earthquakes with non-DC radiation patterns in the upper crust [Frohlich, 1994]. Short-
162 period non-DC events are commonly observed within geothermal areas, such as in Iceland
163 [Foulger and Long, 1984] and California [Ross et al., 1999; Foulger et al., 2004]. Tensile
164 faulting was reported from a geothermal field in West Bohemia, Czech Republic [Vavryčuk,
165 2002], mixed tensile and shear faulting found at Hengill-Grensdalur [Julian et al., 1998],
166 and vertical dipole radiation patterns identified inside the Long Valley caldera [Foulger
167 et al., 2004]. More rarely, implosive earthquakes are recorded in the Námafjall field and the
168 Krafla fires dike zone [Arnott and Foulger, 1994b]. Most of these studies found the non-
169 DC and DC events interspersed in space, and suggested that they are linked to geothermal
170 fluids (circulation of fluids, phase changes, or fluid compressibilities). About 70-75 % of the
171 events at Hengill-Grensdalur in Iceland were classified as non-DC mechanisms with mostly
172 positive volumetric (explosive) components [Miller et al., 1998]. At The Geysers, about
173 50 % have significant volumetric components [Ross et al., 1999] with equal numbers being
174 implosive and explosive. Differences between these two areas are that Hengill-Grensdalur

175 is undeveloped and water-dominated system whereas The Geysers is a steam-dominated
176 and heavily developed system [Ross *et al.*, 1999]. Besides short-period non-DC events,
177 long-period earthquakes are related to fluid-solid interactions with repetitive excitations
178 such as resonance effects of fluid-filled cracks or conduits [e.g., Chouet, 1996; Maeda *et al.*,
179 2013]. Although such signals are observed at Krafla, we do not discuss them here.

180 The pressure (P), neutral (N), and tension (T) orientations, inferred from shear faulting
181 events, were used to interpret the stress orientations in other parts of the North Atlantic
182 ridge [Klein *et al.*, 1977; Foulger, 1988]. They suggest that the least compressive stress
183 (σ_3) is mostly aligned with the spreading direction. The unit eigenvectors of the stress
184 tensor are called the principal stress axes ($\vec{s}_{1,2,3}$) and distinguished from the eigenvalues,
185 which are termed principal stress magnitudes ($\sigma_1 \geq \sigma_2 \geq \sigma_3$) with positive values meaning
186 compression. Arnott and Foulger [1994b] noted a high variability in the P and T axes
187 following the *Krafla fires* rifting episode suggesting that the average deviatoric stresses
188 were small. In the dike zone, the greatest compressive stress (σ_1) was aligned with the
189 spreading direction. This observation let them conceptualise a stress cycle that included
190 inter-rifting ($\sigma_1 \simeq \sigma_2 > \sigma_3$), immediate pre-rifting ($\sigma_1 \simeq \sigma_2 \simeq \sigma_3$), and immediate post-
191 rifting ($\sigma_1 \simeq \sigma_2 \gg \sigma_3$) periods. We analyse and interpret P and T axes orientations of
192 events recorded 25 years after the last rifting episode.

4.1. Calculating focal mechanisms

193 In addition to wave polarity information, amplitude ratios can help significantly to con-
194 strain the inversion of focal mechanisms [Ross *et al.*, 1999]. We prepared the amplitudes
195 such that the signals of the manually picked events are rotated into the ray-frame to
196 analyse compressional and shear waves separately. Incidence and azimuthal angles were

197 obtained from 3D ray tracing the velocity model using an eikonal solver [*Vidale*, 1988;
198 *Hole and Zelt*, 1995]. These angles were compared to angle estimates obtained by parti-
199 cle motion analysis. We found that the incidence and back-azimuth angles retrieved by
200 particle-motions mostly deviated less than 16° and 9° , respectively, from the ray-based
201 estimates. Thereafter, the velocity recordings were transformed to displacement. We
202 followed *Boore* [2003] in compensating for path effects using the 3D ray paths and an ef-
203 fective seismic quality factor of 50. Based on *Schuler et al.* [2014], we regard this value as
204 a reasonable estimate for a sequence comprising layered basalt flows, hyaloclastites, and
205 intrusive rocks. We manually picked the *P*-wave first arrival polarities on the unfiltered
206 data to avoid interpreting the filter imprint. The peak amplitudes of the *P*- and *S*-wave
207 first arrivals, however, were determined on traces convolved with a Butterworth response
208 of order 2 (corner pass-band frequencies at 1.5 Hz and 22 Hz). The polarity orientations
209 of the receivers were verified by teleseisms.

210 Rock anisotropy, strong seismic attenuation and other lateral heterogeneities are charac-
211 teristic for volcanic areas and may affect our arriving amplitudes and introduce errors into
212 the source inversion [*Frohlich*, 1994], but they can be difficult to measure [*Pugh et al.*,
213 2016]. Therefore, we use amplitude ratios in the source inversion where available, as these
214 are less sensitive to path effects. A Bayesian approach is used for moment tensor source
215 inversion by following *Pugh et al.* [2016], which allows rigorous inclusion of both measure-
216 ment and location uncertainties in the resultant probability density function (PDF). The
217 inversion approach determines the probability distribution over the moment tensor space
218 given the observed data. *P*-wave polarities can be combined with the corrected amplitude
219 ratios to determine the source radiation pattern. The inversion was run twice, initially

220 constrained to the DC space and then over the full range of moment tensor solutions,
221 allowing non-DC components to be constrained along with an estimate of whether the
222 source can be described by a DC source or not.

4.2. Estimating crustal stress or deformation rate

223 The first motions recorded at seismic stations are directly linked to the displacement
224 on the fault. The local principal strain rate axes are always 45° inclined from the shear
225 plane regardless of the rock properties (i.e., cohesion). These define the P and T axes.
226 They are found by calculating the best match to the first motions and amplitude ratios.
227 The principal stress directions $\vec{s}_{1,2,3}$ may be considered aligned with the P , N , and T axes.
228 This assumption introduces a stress direction uncertainty of $\pm 15^\circ$ [C  l  rier, 2008]. DC
229 focal solutions can be used to invert for a uniform stress field, but the model requires the
230 faults to occur on randomly oriented planes of weakness (pre-existing faults) and that the
231 material behaves isotropically and linearly. Furthermore, the focal solutions need to show
232 enough orientation diversity with the fault slip parallel to the maximum resolved shear
233 stress, and that the movement of one fault does not influence the slip direction of others. We
234 invert for a uniform stress field using the SATSI algorithm [Hardebeck and Michael, 2006]
235 by exploiting the fact that such a stress field applied to randomly oriented faults leads to a
236 range of DC solutions [McKenzie, 1969]. Strike, dip direction and dip angles of randomly
237 picked DC nodal planes are provided as input. Based on the nodal plane ambiguity
238 angle of about 20° , we verified that the focal diversity is sufficient to resolve the stress
239 orientation. The inversion result represents the best-fitting orientation of the principal
240 stress axes and the relative stress magnitude ratio $R = (\sigma_1 - \sigma_2)/(\sigma_1 - \sigma_3)$, which describes
241 the shape of the stress ellipsoid. Another model exists contrasting the uniform stress

242 model. It assumes that crustal stress is heterogeneous, but exhibits uniform frictional
243 strength [*Smith and Heaton, 2006*]. The evolution of such heterogeneous crustal stresses
244 may be formed by dislocation-velocity-weakening (Heaton pulse) ruptures [*Heaton, 1990*].
245 As *Rivera and Kanamori [2002]* suggested, both models are end-members and the real
246 Earth likely shows characteristics of both models.

247 An alternative view is that fault slip inversions reliably constrain the strain rate or, more
248 accurately, the deformation rate. Here, we mainly follow the arguments of *Twiss and*
249 *Unruh [1998]*. The cumulative effect of many displacements (faults) over a larger volume
250 can be regarded as a small continuum deformation. Inverting the P and T axes thus gives
251 most directly information about the deformation rate, which is related to stress via the
252 rheological properties of the rock. One of the drawbacks in both stress and deformation-
253 rate approaches is that if the medium has preferred shear plane orientations (zones of
254 weaknesses), the inverted global, in contrast to the local, P - and T - axis solutions are
255 likely to be biased, because they do not have to be perpendicular, whereas the principal
256 stress or deformation-rate axes do [*Twiss and Unruh, 1998*].

5. Results

257 Most of the detected seismicity is concentrated in the geothermal fields and in the up-
258 permost 2 – 3 km of the crust (Figures 2a-c). The largest number of events occur at about
259 1.5 km depth bsl with a relatively steep drop at greater depths (Figure 2d). Collecting
260 events only within a radius of 250 m of the IDDP-1 borehole reveals a sharp drop of
261 seismicity below the depth where melt was encountered (Figure 2e). A recovered thermal
262 profile by *Friðleifsson et al. [2015]* is overlain, where superheated steam reaches about
263 500 °C at the bottom of IDDP-1 and the melt temperature is expected to be around

264 900 °C.

265 On average we detected 8 events per day above magnitude -0.6 in the first 319 days and
266 typically 1-2 events every day above magnitude -0.1 in the second 675 days of recording
267 (Figure 2f). The rate change of the total number of recorded earthquakes coincides with
268 a change in the network density. Nine periods are identified with increased seismicity
269 rates of more than 50 additional earthquakes per day (Figure 2e). Two swarms occurred
270 in August 2009, several larger and smaller ones in 2010, and two (not shown here) in
271 2011. We describe below the borehole activity preceding the four swarm periods marked
272 in Figure 2f, but with more focus on the first one that serves as an example. Borehole
273 activity data are compiled by *Ágústsson et al.* [2012] and *Friðleifsson et al.* [2015], as
274 well as received by the well operator Landsvirkjun (pers. comm. S.H. Markússon, 2016).
275 Boreholes that injected relatively constant amounts of fluids are KJ-26 ($0.08\text{-}0.09\text{ m}^3/\text{s}$),
276 KJ-11 ($0.0085\text{ m}^3/\text{s}$), KJ-38 ($0.020\text{-}0.026\text{ m}^3/\text{s}$) and some in KJ-35. The temperature of
277 injected fluids is about 126°C at KJ-26/11. Preceding swarm 1 is a fluid injection stop
278 of $0.025\text{ m}^3/\text{s}$ at IDDP-1 on the 11th of August and deepening of borehole KT-40 between
279 the 13-29 of August. Events of swarm 1, located within cluster E of Figure 2a, were man-
280 ually picked and re-located around KT-40. Small event magnitudes with low SNR led to
281 large picking uncertainties. Circulation losses are reported at KT-40 and the drill bit got
282 stuck multiple times. Attempts to loosen the drill bit by pulling up the drill string and
283 the detonation of three small explosives [*Mortensen et al.*, 2009] caused some better SNR
284 events. We tried to use these arrivals to verify whether our velocity model is reasonable.
285 A relocated event, originating from an attempt to loosen the stuck drill string, is shown
286 in Figures 2a-c. The match between the well trajectory and the relocated hypocenter is

287 within the location uncertainty.

288 Swarms 2 and 3 occur after periods when KT-40 was closed and re-opened, and KJ-39
289 was closed in January and early February 2010. Swarm 4 matches the date when a fluid
290 discharge test was performed on IDDP-1. KJ-39 was closed six days before this test.

291 We sporadically observe small-amplitude aftershocks in the coda of larger-amplitude earth-
292 quakes, but more frequently, we identify events with similar waveforms and magnitudes,
293 sometimes separated only by a few seconds (Figure 3a). They share a common hypocenter
294 location within error bars as well as near-identical source mechanism. We refer to them as
295 multiplets, whose main differences consist of phase delays arising from slightly diverging
296 ray paths. We performed waveform correlations on earthquakes identified by CMM and
297 grouped those that had cross-correlation coefficients above 0.85 on at least two stations.

298 Lower coefficients often retain earthquakes in a similar waveform group with hypocenter
299 locations not explainable by the estimated ± 150 m location uncertainty. A 4 s-long time
300 window, starting at the *P*-wave arrival, was chosen for correlation to include both *P*-
301 and *S*-wave arrivals and some coda signal. We band-pass filtered the vertical component
302 signals 2-18 Hz to reduce noise. On average, 32 % (range 25-45 %) of the earthquakes
303 have at least one other similar event within our recording period. The wide percentage
304 range mainly results from a few stations having significant data gaps at times. Figure
305 3a illustrates example waveforms of multiplets occurring within seconds of one another
306 and that have their hypocenters located in the seismicity cluster A at 1.8 km depth bsl
307 (Figures 2a-c). Another example of multiplets that have longer inter-event times is shown
308 in Figure 3b. Seven matching signals are aligned in time and occurred weeks to months
309 apart from one another as we found is typical for our multiplets. Their source location

310 lies about 100 m SE of the IDDP-1 borehole at 1.5 km depth bsl.

311 The spatial clustering of events at Krafla allows us only to map magnitude distributions
312 in specific areas within the caldera. We selected earthquakes within spheres of two sizes
313 having diameters of 1.0 km and 1.5 km and centered at nodes separated by 125 m. No
314 significant changes are observed regarding the choice of the two sphere sizes and cell node
315 separation other than a smoothing effect. We separately prepared maps for the 319-day
316 and 675-day long periods, because they have different network configurations and have
317 average inter-station distances of 1.5 km and 2.0 km, respectively. The majority of their
318 b -values match within their errors. Therefore, we measure no significant temporal b -value
319 change. Therefore, we cautiously combine the two earthquake catalogues to estimate the
320 size distribution at each node using the higher $M_{\min} = M_c - \Delta M/2$ value that resulted
321 from the two separate time period analyses. An average M_{\min} of -0.6 ± 0.1 and -0.1 ± 0.1
322 were estimated for all the nodes in the 319- and 675-day periods, respectively. We attribute
323 the increased M_{\min} for the later period mainly to the increased inter-station spacing, be-
324 cause calculating M_{\min} for shorter time segments within the two analysis periods and
325 locally at selected nodes returned similar values. In Figure 4, the b -value and error map
326 is generated using the combined catalogue of two recording periods. A sphere radius of
327 0.5 km and a minimum of 100 earthquakes per node were required for populating a node
328 with a value. We observe elevated values at the edges of the colored patches, which are
329 caused by rapidly decreasing earthquake numbers. The reduced number of events within
330 the analysis volumes (spheres) correspond to increased errors in estimating b . Instead of
331 selecting all events within an analysis volume, a constant number of events may be cho-
332 sen randomly or with increasing time until a defined number is reached. This approach

333 reduces edge effects, but may also select events distant from the node center that are then
334 representing the size distribution of that node.

335 *Kamer and Hiemer* [2015] presented a b -value estimation method that explores the model
336 complexity given the data. An advantage of this approach is that every earthquake is used
337 only once to compute a b value within a cell of a node. We select the models giving a
338 better fit to the data than the initial model, which includes events of the entire region
339 to calculate one b value. Instead of dividing the surface area into cells, we segment the
340 depth profile, shown in Figure 4d, into cells such that we can apply the method in 2D.
341 All selected models are used then to build ensemble averaged b -values. We found no sig-
342 nificant spatial pattern. Likewise, selecting a test volume at the bottom of IDDP-1 did
343 not return elevated b values above 1.

344 An average $b = 0.79 \pm 0.04$ ($-0.4 \leq ML \leq 2.0$) of the entire region was estimated incor-
345 porating the entire recording period. We have removed events that significantly exceed
346 the average daily event rate from the earthquake catalogue (i.e., swarms) and recalculated
347 the regional b -value. A $\Delta AIC < 2$ suggests that the removal of these earthquakes does
348 not affect our regional estimate.

349 Only events that have at least 12 polarity picks at distant stations are selected for fur-
350 ther interpretation to ensure a minimum coverage of the focal spheres. More than three
351 quarters of them are located deeper than 1.4 km bsl and the majority have magnitudes
352 above -0.2. This is in agreement with our observation that larger magnitude events occur
353 closer to the depth of the peak seismic activity. Example DC solutions are illustrated in
354 Figures 5a-c with black lines indicating possible DC nodal planes and triangles marking
355 the polarity picks (up or down) at different stations. On the sides of the hemisphere plots,

356 lune source-type plots [*Tape and Tape*, 2013] allow us to visually relate the retrieved mo-
357 ment tensors to an appropriate physical source mechanism. The diagram's center, top,
358 and bottom represent DC and purely explosive and impulsive mechanisms, respectively.
359 Colored dots show the PDF of the solution with red colors marking higher and blue lower
360 probability. The PDF spread reveals that we need well-constrained focal solutions to
361 uniquely assign a physical source mechanism to an event. Figures 5a-b show near-vertical
362 dip-slips, and (c) a normal faulting mechanism. The latter is less well constrained and
363 has two similarly-fitting fault plane pairs with different strike directions. This event is
364 counted as a DC mechanism, but its best fitting strike angle is not used further.

365 A ternary diagram (Figure 6a) provides some quantitative information about the DC fault-
366 ing style of earthquake clusters. We assume close Andersonian faulting, although some
367 non-optimally oriented fault reactivations may lead to inaccurate faulting style represen-
368 tations on the ternary diagram [*Célérier*, 2010]. We find that most events in clusters A-D
369 show normal faulting. Separately analysing individual spatial clusters or grouping the
370 events into different depth bins did not reveal a coherent change of pattern. We followed
371 *Frohlich* [2001] in dividing the focal solutions into four different regimes: normal, reverse,
372 strike-slip, and *odd*. Few solutions exhibit strike-slip or reverse faulting characters. Solu-
373 tions that do not fall into a corner region are termed *odd* and represent oblique-slip on
374 steep planes or strike-slip on low-dipping planes. Several of these *odd* solutions are found
375 close to the T axis with near-vertical or near-horizontal nodal planes. Rose diagrams
376 of their strike directions, grouped according to their spatial clusters, present a diverse
377 distribution (Figures 6b-d). In cluster D, the strikes are mostly parallel in northeastern
378 and southern directions. Clusters A-B are not as clear, but we have here only a few data

379 points.

380 The estimated strike, dip, and rake information were inverted to obtain a uniform stress
381 field orientation for clusters A and B (Figure 7). The grouping of spatially separate event
382 clusters was performed visually. Cluster D in Figure 2a is split into a northwestern (D-
383 NW) and southeastern (D-SE) part. We randomly selected one of the two fault planes
384 to be the correct one. Cluster D-NW mainly covers the surface area between boreholes
385 KJ-26 and IDDP-1. Figures 7b-e show the stress inversion results along with the P and T
386 axes of the individual earthquakes. Colored points in the background represent solutions
387 that are obtained by bootstrap resampling the dataset. Large spreads correspond to less-
388 constrained solutions of $\sigma_{1,2,3}$. The two separate clusters A and B show similar principal
389 stress axis directions, but only a few events are selected. The principal axes cannot be
390 resolved clearly for D-NW and are weakly constrained for D-SE. In all areas the largest
391 compressive stress direction (σ_1) is near vertical. σ_2 and σ_3 in the D subclusters, however,
392 appear to have similar magnitudes, which are reflected in the relatively high value of R as
393 well as in the wide distribution of the σ_2 and σ_3 solutions generated during the bootstrap
394 resampling.

5.1. Non-double couple mechanisms

395 About 10 % of events in cluster A, 17 % in cluster B, and 18 % in cluster D show
396 non-DC source mechanisms. Cluster C had only a handful of events. We obtain these
397 numbers by visually checking the lower hemisphere projections of forced DC solutions and
398 also the spread of uncertainty (95 % contour interval) in the lune source-type plots. We
399 only counted an event as non-DC, if the 95 % contour interval of the uncertainty map
400 did not overlap with the DC point in the lune plot. Sole inspection of the lune diagram

401 would, of course, not allow a decision to be made as to whether an event is DC or not.
402 We may have picked only positive polarities in the compressional, or negative polarities
403 in the dilatational, quadrants indicating a pure isotropic source in the lune plot, although
404 it may be a DC event. We further find that one third of the non-DC events in cluster A,
405 18 % in cluster B, and 30 % in cluster D show negative volumetric components.
406 Locations of sources with large volumetric changes and no opposite polarity picks are
407 shown in Figures 2a-c. Most non-DC sources are explosive, with only two being implosive.
408 We note that these events lie locally below the deepest points of the nearest boreholes.

6. Discussion

409 The seismicity in 2009-2012 was governed by small-magnitude events during a volcani-
410 cally quiet period. An estimated 32 % of the earthquakes are repeating events. This
411 clustering rate fits well the rates of 24-37 % reported from other active volcanic caldera
412 systems, which have events with similar magnitudes (*Massin et al.* 2013 and references
413 therein). The non-repeating events may represent ruptures of partially-healed pre-existing
414 faults or intact rock. Considering the magnitudes of our events, typical source dimensions
415 of up to a few tens of meters can be expected [*Wyss and Brune*, 1968]. Circulating
416 geothermal fluids possibly limit crack propagation during earthquake ruptures and hence
417 their size [*Foulger and Long*, 1984]. We find a weak correlation between increased numbers
418 of multiplets and swarms. The average magnitudes of repeating events is 0.1 ± 0.5 (2061
419 events) and for swarms -0.2 ± 0.4 (703 events). The weak correlation between increased
420 numbers of multiplets and swarms is used sometimes to argue that the locally modified
421 stresses leading to swarms re-activated pre-existing faults.

422 We observe that swarms often occur simultaneously or days after fluids have been in-

423 jected, the injection rate changed, or circulation losses occurred while drilling. Fluid
424 re-injection started in 2002 at Krafla partly in an attempt to sustain reservoir pressure.
425 *Ágústsson et al.* [2012] noted that induced seismicity occurred as soon as more than 0.04-
426 0.06 m³/s were injected at Krafla. Circulation fluids lost during drilling reached volumes
427 up 0.04 m³/s [*Mortensen et al.*, 2009]. We also observe elevated seismicity when larger
428 volumes are injected. Small injection volumes probably cause smaller magnitude events
429 or aseismic slip. We observe little swarm activity during periods when little or no change
430 in fluid balance occurs. This suggests that fluids are likely candidates for the triggering
431 microearthquakes. In the case of injections, fluids locally increase the pore pressure and
432 reduce the effective normal stresses on nearby faults and so bring them closer to failure
433 [*Raleigh et al.*, 1976].

6.1. Earthquake size distribution

434 Our b -values (Figure 4) of the Krafla caldera indicate normal crustal values, which match
435 the findings of *Arnott and Foulger* [1994a] twenty years earlier. It appears that the b -values
436 are not elevated despite the presence of melt at shallow depth, associated high geothermal
437 gradients and pore pressures, and sequences of extensively fractured rocks. Possibly we are
438 observing the third stage of the characteristic b -value sequence, described earlier, where
439 intrusive melt has been sitting in the crust for some time and the initially increased pore
440 pressure due to magmatic degassing and hot geothermal fluids has reached a relatively
441 constant level. In the case of a long-lived melt body beneath Krafla, the concentrated
442 stress introduced during earlier dike formation may have been dissipated through on-going
443 rifting. An alternative explanation for the low b -values is that the melt pockets are small
444 localized features that do not cause increased small-magnitude seismicity. However, this

445 would not be in agreement with tomographic images [e.g., *Schuler et al.*, 2015] and the
446 fact that heat is expelled over large surface areas. Our preferred explanation therefore is a
447 larger single, or multiple smaller melt bodies, embedded in a hot and plastically-behaving
448 crust.

6.2. Double-couple earthquakes

449 Most of the focal solutions in Figure 6a exhibit normal faulting characteristics. The
450 strike azimuths appear scattered, but nonetheless show a slight dominance in NE-SW and
451 E-W directions. Both observations agree with results presented by Arnott and Foulger
452 [1994b]. A fast shear-wave polarisation analysis by *Tang et al.* [2008] found two preferred
453 fast-polarisation directions, N-S and E-W, which were interpreted as two fracture systems
454 oriented perpendicular to each other.

455 Inverting focal solutions for a uniform stress field has limitations. A uniform stress field
456 is perhaps a good assumption in some regions [*Zoback and Zoback*, 1980], but may give
457 meaningless results in others [*Smith and Heaton*, 2006]. If a new fault plane develops
458 in isotropic rock with a uniform background stress field, the P and T axes may give an
459 indication of \vec{s}_1 and \vec{s}_3 , respectively. In more realistic settings, slip frequently occurs on
460 non-optimally oriented, pre-existing planes of weaknesses. We find that at least one third
461 of events at Krafla are repeating events. *C  lerier* [2008] proposed that re-activated faults
462 are more likely to be near-optimally oriented if they plot closer to the corners in a ternary
463 diagram (Figures 7b-e). However, selecting only these events to invert for stress directions
464 would reduce the focal diversity needed to solve for the principal stress axes.

465 *Wyss et al.* [1992] argue that it is reasonable to assume a uniform stress field if sub-
466 volumes of data return similar results. The small number of earthquakes prevents us

467 from dividing our clusters into smaller volumes except for cluster D. Clusters A and B
468 exhibit similar stress orientations with σ_1 pointing vertically down and σ_3 being parallel
469 to the spreading direction. These axis orientations coincide with the classical model of an
470 extensional tectonic stress regime where $\sigma_1 \simeq \sigma_2 > \sigma_3$. Similar results have been reported
471 from other parts of the rift axis [e.g., *Klein et al.*, 1977; *Foulger*, 1988]. Hydro-fracturing
472 borehole stress measurements in east Iceland show that the maximum horizontal stress is
473 sub-parallel to the nearest fissure swarms in the axial rift zone and thus the minimum hori-
474 zontal stress is sub-parallel to the spreading direction [*Haimson and Rummel*, 1982]. They
475 also show that horizontal stresses increase slowly with depth and that the vertical stress
476 becomes larger at a few hundred meters depth, leading to optimal conditions for normal
477 faulting. Borehole pressure logs from IDDP-1 show a pivot point at 1.95 km depth with
478 a pressure of 15.5 MPa [*Friðleifsson et al.*, 2015]. The pivot point, usually representing
479 the depth of the dominating formation feeding zone, determines the formation pressure at
480 that depth. Near crystallizing and cooling magma walls, significant tensile stresses may
481 develop with \vec{s}_3 perpendicular to the lithostatic load, whereas below the brittle-plastic
482 transition we expect the lithostatic load to become σ_3 due to the deformation in response
483 to buoyancy [*Fournier*, 1999].

484 Cluster D-NW and D-NE exhibit near-vertical σ_1 , but σ_2 and σ_3 appear to be different
485 than in clusters A and B (Figure 7). Cluster D-NW is especially unconstrained as is indi-
486 cated by the large spread of solutions generated during bootstrap resampling. Perhaps this
487 shows that $\sigma_2 \approx \sigma_3$. In contrast to the volumes of clusters A and B, D mostly encompasses
488 the exploited geothermal field undergoing fluid injections/withdrawals. Two active wells,
489 KJ-26 and IDDP-1, both penetrate the volume of cluster D-NW. Earthquakes used for our

490 stress analysis all originate from a similar depth range, which is dominated by intrusives at
491 the IDDP-1 site. In contrast to our horizontal stress change indications, *Martínez-Garzón*
492 *et al.* [2013] reported vertical stress changes between reservoir and adjacent hostrock at
493 The Geysers likely induced by poroelastic or thermoelastic stressing. Around producing
494 fractures, where strong temperature and pressure gradients are expected, thermoelastic
495 effects may dominate over poroelastic effects and alter the stress state within the reservoir
496 [*Segall and Fitzgerald*, 1998].

497 For the Bjarnarflag-Námafjall field and the dike zone, Arnott and Foulger [1994b] found
498 just after the *Krafla fires* rifting episode that the stress orientations were highly variable
499 and \vec{s}_1 was perpendicular to the rift axis. The latter was possibly caused by multiple
500 intrusions and caused \vec{s}_1 to rotate from vertical to horizontal. About twenty years after
501 the *Krafla fires* and about 5 km to the north along the rift axes, we find \vec{s}_1 vertical inside
502 and outside the main exploited geothermal field. \vec{s}_3 is nearly aligned with the spreading
503 direction outside the main geothermal field and oriented as imagined during an inter-
504 rifting period [Arnott and Foulger, 1994b]. *Bergerat et al.* [1990] and *Plateaux et al.*
505 [2012] also found σ_3 aligned parallel to the plate divergence direction both in and off the
506 rift zone for locations to the north, south, and east of Krafla. The horizontal stress axes
507 in the lower part of the productive field suggest $\sigma_2 \approx \sigma_3$. We know further from geodetic
508 measurements [*Ali et al.*, 2014] that the observed surface deformation is attributed to the
509 half-spreading rate of 9 mm/yr of the plates, viscoelastic relaxation deriving from the
510 Krafla fires, and a shallow deflating magma reservoir. Therefore, the local stress field may
511 be affected by a more complex interaction of different stress sources.

512 If we apply the deformation rate interpretation of slip inversion data, the global P and

513 T axes are not interpreted as \vec{s}_1 and \vec{s}_3 but instead as the most and least compressive
514 deformation rate directions. The smallest deformation rate axis is closely aligned with
515 the spreading direction in clusters A and B, somewhat diffuse in D-NW, and parallel to
516 the rift in D-SE. Local fault block rotations during slip are not considered here.

6.3. Non-double-couple earthquakes

517 A large proportion of events are consistent with non-shear faulting behavior. Similar
518 to previous studies, we found numerous non-shear events at Krafla interspersed with DC
519 earthquakes. However, we classified less than 20 % as distinct non-shear events, of which
520 most are explosive and have magnitudes between -0.3 and 0.6. In comparison to some
521 other studies, we believe this low percentage partly derives from including uncertainties
522 in the moment-tensor inversion and partly because we sometimes suffer from sparse focal
523 coverage. Nevertheless, there is tensile and tensile-shear faulting occurring close to the
524 brittle-plastic transition. Ground water is heated and expands to a high-pressured and
525 superheated fluid near the melt leading to hydraulic fracturing and brecciation. Exsolving
526 magmatic fluids, comprising hypersaline brine and steam, are expected to cross the brittle-
527 plastic interface on occasion. Pore pressures in the plastic rock are equal to the lithostatic
528 load but are hydrostatic in the brittle environment, which will cause the fluid to expand
529 and transform to superheated steam when moving into the brittle part [*Fournier, 1999*].
530 The decompression causes brecciation, an increase in the strain rate, and stress difference
531 in the plastic rock due to increased fluid movement across the brittle-plastic interface
532 [*Fournier, 1999*]. The fact that superheated fluids are extracted from a highly productive
533 zone overlying melt suggests that this is a reasonable conceptual model for this zone.
534 The non-DC earthquakes are expected to occur in this zone, where fluid can change the

535 ambient stress locally, and cracks may open or close, or even remain open.

536 We recorded two mainly-implosive events that might be related to thermal contraction
537 of cooling magma [Foulger and Long, 1984; Miller et al., 1998] underneath. One of these
538 implosive events is less than 300 m south of IDDP-1 and therefore close to where we expect
539 the melt-rock interface to lie (Figure 2a-c). The second is located at the bottom of the
540 seismicity cluster A to the NW, which shows the same characteristic seismicity distribution
541 as at IDDP-1. Thus, we believe that this event is also located close to an underlying
542 melt zone. This is supported by tomographic images [Schuler et al., 2015]. A source
543 dominated by near-vertical single force or a vertical-CLVD mechanism might produce only
544 dilatational first motions as well at the stations, but this presumes that there is a small
545 region at the surface where we could have recorded compressional first motions. Physical
546 sources for such mechanisms may include fluid movement or cone-shaped fault structures
547 [Schuler et al., 2013]. Although we cannot rule out such an alternative explanation, we
548 stick with the simple implosive source explanation. Fluid motions, phase changes, mixing
549 of meteoric and magmatic fluids, and cooling of the underlying magma pocket are likely
550 to be responsible for the variety of DC and non-DC earthquakes. Seismogenic faulting
551 within the highly viscous silicic magma may also produce earthquakes with magnitudes
552 that would be observable with our network [Tuffen et al., 2008]. However, our location
553 uncertainties do not allow us to pinpoint the hypocenters exactly to one stratigraphic
554 layer, because the whole vertical sequence at the bottom of IDDP-1, comprising dolerites,
555 granophyres (highly productive zone) and rhyolitic melt is only about 100 m thick.

556 On a final note, crustal anisotropy has not been considered in our tomographic model
557 nor in our focal mechanism inversions. We expect, however, from shear-wave splitting

558 measurements [*Tang et al.*, 2008] and from the aligned fractures in the extensive fissure
559 system at the surface, that the crustal fabric is anisotropic. This in turn must affect
560 our moment tensor inversion [*Vavryčuk*, 2005]. We have not included nor assessed this
561 uncertainty yet.

7. Conclusion

562 The microseismicity within the Krafla caldera between 2009 and 2012 is concentrated
563 near geothermal fields in the upper 2-3 km. The depth with the largest number of earth-
564 quakes above the magnitude of completeness matches the depth of the rock-melt interface
565 at the IDDP-1 borehole. The relative size distributions of events (b -value) are not elevated
566 close to the melt, but rather show average crustal values of $b \leq 0.9$. Although this is a
567 period of volcanic quiescence, a few small-magnitude earthquake swarms were detected
568 at locations and times suggesting that geothermal fluids are important in the triggering
569 processes. A weak correlation between swarms and repeating earthquakes is interpreted
570 as stress activation of pre-existing faults. About 32 % of the events are found to be re-
571 peating earthquakes.

572 Focal solutions of earthquakes suggest that less than about 20 % deviate significantly
573 from shear-faulting mechanisms. Most non-shear mechanisms involve positive volume
574 changes and only two were implosive events. The proximity of these events to the ex-
575 pected melt-rock interface depth suggests that geothermal fluids play an important role
576 in their source processes. We surmise that they occurred in the superheated steam zone
577 above the melt. The double-couple earthquakes, on the other hand, mostly represent
578 normal faulting styles. Estimated P and T axes were used to infer the principal stress or
579 deformation rate axes. We find that the maximum compressive stress (deformation rate)

580 axis is always vertical. The least compressive stress (deformation rate) direction is closely
581 aligned with the plate spreading direction outside the main geothermal field and is not
582 well defined inside it. Here, the relative horizontal stress (deformation-rate) magnitudes
583 are similar.

8. Figure Captions

584 1. Map of the study area. Station locations are marked by green triangles, the mapped
585 caldera rim in red, the IDDP-1 well as white cross, and manually picked earthquakes
586 with yellow circles. Our local analysis grid is colored in blue and lava flows of the Krafla
587 fires are shaded in dark grey. Inset A shows a map of Iceland, the location of the Krafla
588 volcano (box) in the Northern Volcanic Zone (NVZ), and the fissures of the volcanic
589 systems (purple lines) delineating the plate boundary. Inset B is an enlarged map of the
590 central caldera.

591 2. (a) Map of the central caldera and earthquake distribution recorded in 2009-2012.
592 The *Krafla fires* lava flows, Víti crater lake, road, and power plant are shaded in dark
593 grey. (b-c) Depth sections of the event distribution and trajectories of all wells. (d-e)
594 Histograms illustrating the number of events versus depth. The number of events within
595 a radius of 250 m of the IDDP-1 well are displayed in (e) along with the thermal recovery
596 profile (black line). Horizontal arrows mark the depths where melt was encountered. (f)
597 Histograms with one-day event bins in the area outlined in (a-c) but for only the period
598 where we have injection volume data. Labelled arrows indicate swarms discussed in the
599 text. The average injection rate of the main injection well KJ-26 at Krafla is superimposed
600 (dashed blue line) after *Ágústsson et al.* [2012].

601 3. (a) Earthquakes with similar waveforms recorded at station K090 within seconds
602 of one another. An enlarged signal window and the event focal mechanisms in lower
603 hemisphere equal-area projection are displayed above. Black quadrants contain the tension
604 axes. (b) Seven normalized waveforms from station K100 are aligned on a P -wave arrival
605 (vertical bar). Their ML range between -0.29 and 0.51. Black line represents the stacked
606 waveform. Four well-constrained focal solutions of the events are shown above with their
607 origin times.

608 4. Size distribution map of the central Krafla caldera including data recorded between
609 September 2009 and July 2012. The b -values were estimated within spheres with radii
610 0.5 km around the cell nodes. The nodes, marked as squares, are separated by 125 m. A
611 minimum number of 100 events was requested to populate a node. Surface locations of
612 all geothermal wells and the trajectories of IDDP-1 and KJ-39, which both drilled into
613 melt, are colored in pink.

614 5. (a-c) DC focal mechanisms displayed in lower hemisphere projections on their left,
615 with stations (triangles) indicating their polarity picks (up, down) of the arriving wave-
616 forms. Black lines show the distribution of possible fault planes for DC-constrained solu-
617 tions. On their right, lune source-type plots [*Tape and Tape*, 2013] of the PDF are plotted
618 with blue colors corresponding to low and red to high probability. Event (d) illustrates
619 a strongly implosive event and (e) an explosive event with all arrivals having the same
620 polarities. Details of the event magnitudes and locations are given below subfigures in
621 (a-c) and on their sides in (d-e).

622 6. (a) Equal-area projection, after *Kaverina et al.* [1996], displaying the distribution
623 of 182 well-constrained DC focal mechanisms (dots). Dot sizes are scaled relative to

624 their event magnitudes. Compressed quadrants of the beachball plots are colored black.
625 Following *Frohlich* [2001], we further delineate corner regions in which faulting mechanisms
626 are considered predominantly as normal, reverse (thrust), and strike-slip. Curved lines
627 indicate where the P , N , and T axes lie within 30° , 30° , and 40° of the vertical, respectively.
628 (b-d) Rose diagrams that show the strike directions of well-constrained DC nodal planes.
629 Cluster letters and number of events are given below the plots.

630 7. (a) Map showing the hand-picked earthquake epicenters (circles), fissures (purple
631 lines, after *Hjartardóttir et al* [2012]) used as a proxy of the rift axis, caldera rim (red), and
632 the dike zone (green) of the *Krafla fires*. (b-e) Lower hemisphere equal-area projection of
633 P (open circles) and T (black solid points) axes of well-constrained DC events for clusters
634 A, B, D-NW, and D-SE. The selected events are highlighted in (a). Red (\vec{s}_1), green (\vec{s}_2),
635 and blue (\vec{s}_3) crosses represent the best-fitting principal stress axes. R is the relative
636 stress magnitude. Color-coded circles mark stress axes solutions obtained by bootstrap
637 resampling 1000 times.

638 **Acknowledgments.** We thank Julian Drew for the use of his CMM algorithm and
639 Jon Tarasewicz for acquiring the bulk of the field data. Seismometers were borrowed
640 from SEIS-UK under loan 891, with additional data from SIL network stations operated
641 by the Icelandic Meteorological Office. The data will be stored at IRIS (www.iris.edu)
642 and accessible from there. The Natural Environment Research Council UK funded the
643 fieldwork. Landsvirkjun supported the field campaigns and provided borehole information.
644 We thank two anonymous reviewers for critically reading this paper. J.S. also thanks Y.
645 Kamer and S. Hiemer for discussing parts of their b -value method. Data were mainly

646 processed using the ObsPy package and visualized using Matplotlib and Generic Mapping
647 Tools. J.S. was supported by the Swiss National Science Foundation.

References

- 648 Ágústsson, K., Ó.G. Flóvenz, Á. Guðmundsson, and S. Árnadóttir (2012), Induced seis-
649 micity in the Krafla high temperature field, *GRC Transactions*, *36*, 975–980.
- 650 Akaike, H. (1974), A new look at the statistical model identification, *IEEE Trans. Au-*
651 *tomat. Contr.*, *19*, 716–723.
- 652 Ali, S.T., K.L. Feigl, B.B. Carr, T. Masterlark, and F. Sigmundsson (2014), Geodetic mea-
653 surements and numerical models of rifting in Northern Iceland for 1993-2008, *Geophys.*
654 *J. Int.*, *196*, 1267–1280.
- 655 Ármannsson, H., B. Gudmundsson, and B.S. Steingrímsson (1987), Exploration and devel-
656 opment of the Krafla geothermal area, *Jökull*, *37*, 13–29.
- 657 Árnason, K., A.M. Vilhjálmsson, and T. Björnsdóttir (2009), A study of the Krafla volcano
658 using gravity, micro-earthquake and MT data, *Short Course IV on Exploration for*
659 *Geothermal Resources*, United Nations University, Kenya.
- 660 Arnott, S., and G. Foulger (1994), The Krafla spreading segment, Iceland: 1. Three-
661 dimensional crustal structure and the spatial and temporal distribution of local earth-
662 quakes, *J. Geophys. Res.*, *99*, 23801–23825.
- 663 Arnott, S., and G. Foulger (1994), The Krafla spreading segment, Iceland: 2. The accre-
664 tionary stress cycle and nonshear earthquake focal mechanisms, *J. Geophys. Res.*, *99*,
665 23827–23842.

- 666 Bergerat, F., J. Angelier, and T. Villemin (1990), Fault systems and stress patterns on
667 emerged oceanic ridges: a case study in Iceland, *Tectonophys.*, *179*, 183–197.
- 668 Björnsson, A., G. Johnsen, S. Sigurdsson, and G. Thorbergsson (1979), Rifting of the
669 plate boundary in North Iceland 1975-1978, *J. Geophys. Res.*, *84*, 3029–3038.
- 670 Boore, D.M. (2003), Simulation of ground motion using the stochastic method, *Pure and*
671 *Appl. Geophys.*, *160*, 635–676.
- 672 Bormann, P., S. Wendt, and D. Di Giacomo (2013), Summary of magnitude working group
673 recommendations on standard procedures for determining earthquake magnitudes from
674 digital data, IASPEI.
- 675 Brandsdóttir, B., and P. Einarsson (1979), Seismic activity associated with the Septem-
676 ber 1977 deflation of the Krafla central volcano in northeastern Iceland, *J. Volcanol.*
677 *Geotherm. Res.*, *6*, 197–212.
- 678 Brandsdóttir, B., and W. Menke (1992), Thin low-velocity zone within the Krafla caldera,
679 NE-Iceland attributed to a small magma chamber, *Geophys. Res. Lett.*, *12*, 2381–2384.
- 680 Brandsdóttir, B., W. Menke, P. Einarsson, R.S. White R.S., and R.K. Staples (1997),
681 Färoe-Iceland Ridge Experiment 2. Crustal structure of the Krafla central volcano, *J.*
682 *Geophys. Res.*, *102*, 7867–7886.
- 683 Buck, W.R., P. Einarsson, and B. Brandsdóttir (2006), Tectonic stress and magma cham-
684 ber size as controls on dike propagation: constraints from the 1975-1984 Krafla rifting
685 episode, *J. Geophys. Res.*, *111*, B12404, doi:10.1029/2005JB003879.
- 686 Célérier, B. (2008), Seeking Anderson’s faulting in seismicity: a centennial celebration,
687 *Rev. Geophys.*, *46*, 1–34.

- 688 Célérier, B. (2010), Remarks on the relationship between the tectonic regime, the rake of
689 the slip vectors, the dip of the nodal planes, and the plunges of the P, B, and T axes of
690 earthquake focal mechanisms, *Tectonophys.*, *482*, 42–49.
- 691 Chouet, B.A. (1996), Long-period volcano seismicity: its source and use in eruption fore-
692 casting, *Nature*, *380*, 309–316.
- 693 Drew, J., R.S. White, F. Tilmann, and J. Tarasewicz (2013), Coalescence microseismic
694 mapping, *Geophys. J. Int.*, *195*, 1773–1785.
- 695 Einarsson, P. (1978), S-wave shadows in the Krafla caldera in NE-Iceland, evidence for a
696 magma chamber in the crust, *Bull. Volcanol.*, *41*, 187–195.
- 697 Einarsson, P. (1991), Earthquakes and present-day tectonism in Iceland, *Tectonophys.*,
698 *189*, 261–279.
- 699 Einarsson, P., and B. Brandsdóttir (1980), Seismological evidence for lateral magma in-
700 trusion during the July 1978 deflation of the Krafla volcano in NE-Iceland, *J. Geophys.*,
701 *47*, 160–165.
- 702 Elders, W., et al. (2011), Origin of a rhyolite that intruded a geothermal well while drilling
703 at the Krafla volcano, *Geology*, *39*, 231–234.
- 704 Farell, J., S. Husen, and R.B. Smith (2009), Earthquake swarm and *b*-value character-
705 ization of the Yellowstone volcano-tectonic system, *J. Volcan. Geotherm. Res.*, *188*,
706 260–276.
- 707 Fournier, R.O. (1999), Hydrothermal processes related to movement of fluid from plastic
708 into brittle rock in the magmatic-epithermal environment, *Econom. Geol.*, *94*, 1193–
709 1211.

- 710 Foulger, G.R. (1988), Hengill triple junction, SW Iceland: anomalous earthquake focal
711 mechanisms and implications for process within the geothermal reservoir and at accre-
712 tionary plate boundaries, *J. Geophys. Res.*, *93*, 13507–13523.
- 713 Foulger, G.R., B.R. Julian, D.P. Hill, A.M. Pitt, P.E. Malin, and E. Shalev, E. (2004),
714 Non-double-couple microearthquakes at Long Valley caldera, California, provide evi-
715 dence for hydraulic fracturing, *J. Volc. Geotherm. Res.*, *132*, 45–71.
- 716 Foulger, G.R., and R.E. Long (1984), Anomalous focal mechanisms: tensile crack forma-
717 tion on an accreting plate boundary, *Nature*, *310*, 43–45.
- 718 Friðleifsson, G.O., B. Pálsson, A.L. Albertsson, B. Stefánsson, E. Gunnlaugsson, J. Ketils-
719 son, and P. Gíslason (2015), IDDP-1 drilled into magma - World’s first magma-EGS
720 system created, paper presented at World Geothermal Congress 2015, Melbourne, Aus-
721 tralia.
- 722 Frohlich, C. (1994), Earthquakes with non-double-couple mechanisms *Science*, *264*, 804–
723 809.
- 724 Frohlich, C., and S. Davis (1993), Teleseismic b-values: or, much ado about 1.0, *J. Geo-*
725 *phys. Res.*, *98*, 631–644.
- 726 Frohlich, C. (2001), Display and quantitative assessment of distributions of earthquake
727 focal mechanisms, *Geophys. J. Int.*, *144*, 300–308.
- 728 Gutenberg, R., and C.F. Richter (1944), Frequency of earthquakes in California, *Bull.*
729 *Seism. Soc. Am.*, *34*, 185–188.
- 730 Haimson, B.C., and F. Rummel (1982), Hydrofracturing stress measurements in the Ice-
731 land research drilling project drill hole at Reydarfjordur, Iceland, *J. Geophys. Res.*, *87*,
732 6631–6649.

- 733 Hardebeck, J.L., and A.J. Michael (2006), Damped regional-scale stress inversions:
734 methodology and examples for southern California and the Coalinga aftershock se-
735 quence, *J. Geophys. Res.*, *111*, doi:10.1029/2005JB004144.
- 736 Heaton, T.H. (1990), Evidence for and implications of self-healing pulses of slip in earth-
737 quake rupture, *Phys. Earth Planet. Int.*, *64*, 1–20.
- 738 Hole, J.A., and B.C. Zelt (1995), 3-D finite-difference reflection traveltimes, *Geophys. J.*
739 *Int.*, *121*, 427–434.
- 740 Hjartardóttir, Á.R., P. Einarsson, E. Bramham, and T.J. Wright (2012), The Krafla fissure
741 swarm, Iceland, and its formation by rifting events, *Bull. Volcanol.*, *74*, 2139–2153.
- 742 Ishimoto, M., and K. Iida (1939), Observations of earthquakes registered with the micro-
743 seismograph constructed recently, *Bull. Earthq. Res. Inst.*, *17*, 443–478.
- 744 Jacobs, K.M., E.G.C. Smith, M.K. Savage, and J. Zhuang (2013), Cumulative rate analysis
745 (CURATE): a clustering algorithm for swarm dominated catalogs, *J. Geophys. Res.*,
746 *118*, 553–569.
- 747 Jónasson, K. (2007), Silicic volcanism in Iceland: composition and distribution within the
748 active volcanic zones, *J. Geodyn.*, *43*, 101–117.
- 749 Julian, B.R., A.D. Miller, and G.R. Foulger (1998), Non-double couple earthquakes, *Rev.*
750 *Geophys.*, *36*, 525–549.
- 751 Kamer, Y., S. Hiemer (2015), Data-driven spatial b value estimation with applications to
752 California seismicity: To b or not to b , *J. Geophys. Res.*, *120*, 1–24.
- 753 Kaverina, A.N., A.V. Lander, and A.G. Prozorov (1996), Global creepex distribution and
754 its relation to earthquake-source geometry and tectonic origin, *Geophys. J. Int.*, *125*,
755 249–265.

- 756 Klein, F.W., P. Einarsson, M. Wyss (1977), The Reykjanes Peninsula, Iceland, earthquake
757 swarm of September 1972 and its tectonic significance, *J. Geophys. Res.*, *82*, 865–887.
- 758 Maeda, Y., H. Kumagai, R. Lacson Jr., M.S. Figueroa II, and T. Yamashina (2013), Source
759 process of long-period seismic events at Taal volcano, Philippines: Vapor transportation
760 and condensation in a shallow hydrothermal fissure, *J. Geophys. Res.*, *118*, 2832–2846.
- 761 Martínez-Garzón, P., M. Bohnhoff, G. Kwiatek, and G. Dresen (2013), Stress tensor
762 changes related to fluid injection at The Geysers geothermal field, California, *Geophys.*
763 *Res. Lett.*, *40*, 1–6.
- 764 Massin, F., J. Farell, and R.B. Smith (2013), Repeating earthquakes in the Yellowstone
765 volcanic field: Implications for rupture dynamics, ground deformation, and migration
766 in earthquake swarms, *J. Volcanol. and Geotherm. Res.*, *257*, 159–173.
- 767 McKenzie, D.P. (1969), The relation between fault plane solutions for earthquakes and
768 the directions of the principal stresses, *Bull. Seismol. Soc. Am.*, *59*, 591–601.
- 769 McNutt, S.R. (2005), Volcanic seismology, *Annu. Rev. Earth Planet. Sci.*, *33*, 461–491.
- 770 Miller, A.D., G.R. Foulger, and B.R. Julian (1998), Non-double-couple earthquakes, 2.
771 observations *Rev. of Geophys.*, *36*, 551–568.
- 772 Miller, A.D., B.R. Julian, and G.R. Foulger (1998), Three-dimensional seismic structure
773 and moment tensors of non-double-couple earthquakes at the Hengill-Grensdalur vol-
774 canic complex, Iceland, *Geophys. J. Int.*, *133*, 309–325.
- 775 Mogi, K. (1962), Magnitude-frequency relation for elastic shocks accompanying fractures
776 of various materials and some related problems in earthquakes, *Bull. Earthq. Res. Inst.*,
777 *40*, 831–853.

- 778 Mortensen, A.K., Þ Egilson, B. Gautason, S. Árnadóttir, and Á Guðmundsson (2014),
779 Stratigraphy, alteration mineralogy, permeability and temperature conditions of well
780 IDDP-1, Krafla, NE-Iceland, *Geothermics*, *49*, 31–41.
- 781 Mortensen, A.K., K. Grönvold, Á Gudmundsson, B. Steingrímsson, and T. Egilson,
782 (2010), Quenched silicic glass from well KJ-39 in Krafla, north-eastern Iceland, paper
783 presented at World Geothermal Congress 2010, Bali, Indonesia.
- 784 Mortensen, A.K., M.Á. Sigurgeirsson, Þ Egilson, G.H. Guðfinnsson, H. Tryggvason, R.B.
785 Jónsson, and S. Sveinbjörnsson (2009), Krafla áðŠ Hóla KT-40. 3. áfangi: Jarðla-
786 gagreining og mælingar. Krafla - borehole KT-40, 3rd section: Borehole geology and
787 geophysical measurements, *iSOR-2009/70*, *LV-2009/144*, 1–24.
- 788 Plateaux, R., F. Bergerat, N. Béthoux, T. Villemin, and M. Gerbault (2012), Implications
789 of fracturing mechanisms and fluid pressure on earthquakes and fault slip data in the
790 east Iceland rift zone, *Tectonophys.*, *581*, 19–34.
- 791 Pugh, D.J., R.S. White, and P.A.F. Christie (2016), A Bayesian method for microseismic
792 source inversion, *Geophys. J. Int.*, doi: 10.1093/gji/ggw186.
- 793 Raleigh, C.B., J.H. Healy, and J.D. Bredehoeft (1976), An experiment in earthquake
794 control at Rangley, Colorado, *Science*, *191*, 1230–1237.
- 795 Rivera, L., and H. Kanamori (2002), Spatial heterogeneity of tectonic stress and friction
796 in the crust, *Geophys. Res. Letts.*, *29*, doi:10.1029/2001GL013803.
- 797 Ross, A., G.R. Foulger, and B.R. Julian (1999), Source processes of industrially-induced
798 earthquakes at The Geysers geothermal area, California, *Geophys.*, *64*, 1877–1889.
- 799 Sæmundsson, K. (1979), Outline of the geology of Iceland, *Jökull*, *29*, 7–28.

- 800 Scholz, C.H. (1968), The frequency-magnitude relation of microfracturing in rock and its
801 relation to earthquakes, *Bull. Seismol. Soc. Am.*, *58*, 399–415.
- 802 Schorlemmer, D., S. Wiemer and M. Wyss (2005), Variations in earthquake-size distribu-
803 tion across different stress regimes, *Nature*, *437*, 539–542.
- 804 Schuler, J., P.A.F. Christie, R.S. White (2014), Borehole study of compressional and shear
805 attenuation of basalt flows penetrated by the Brugdan and William wells on the Faroes
806 shelf, *Geophys. Prosp.*, *62*, 315–332.
- 807 Schuler, J., T. Greenfield, R.S. White, S.W. Roecker, B. Brandsdóttir, J.M. Stock,
808 J. Tarasewicz, H.R. Martens, D.J. Pugh (2015), Seismic imaging of the shal-
809 low crust beneath the Krafla central volcano, NE Iceland, *J. Geophys. Res.*, *120*,
810 doi:10.1002/2015/JB012350.
- 811 Segall, P., S.D. Fitzgerald (1998), A note on induced stress changes in hydrocarbon and
812 geothermal reservoirs, *Tectonophys.*, *289*, 117–128.
- 813 Shi, Y., B.A. Bolt (1982), The standard error of the magnitude-frequency b -value, *Bull.*
814 *Seism. Soc. Am.*, *72*, 1677–1687.
- 815 Shuler, A., G. Ekström, and M. Nettles (2013), Physical mechanisms for vertical-CLVD
816 earthquakes at active volcanoes, *J. Geophys. Res.*, *118*, 1569–1586.
- 817 Smith, D.E., and T. Heaton (2006), Models of stochastic, spatially varying stress in the
818 crust compatible with focal-mechanism data, and how stress inversions can be biased
819 toward the stress rate, *Bull. Seismol. Soc. Am.*, *101*, 1396–1421.
- 820 Sykes, L.R. (1970), Earthquake swarms and sea-floor-spreading, *J. Geophys. Res.*, *75*,
821 6598–6611.

- 822 Tang, C., J.A. Rial, and J.M. Lees (2008), Seismic imaging of the geothermal field at
823 Krafla, Iceland, using shear-wave splitting, *J. Volcanol. and Geotherm. Res.*, *176*, 315–
824 324.
- 825 Tape, W., and C. Tape (2013), The classical model for moment tensors, *Geophys. J. Int.*,
826 *195*, 1701–1720.
- 827 Tinti, S., and F. Mulargia (1987), Confidence intervals of b values for grouped magnitudes,
828 *Bull. Seismol. Soc. Am.*, *77*, 2125–2134.
- 829 Tuffen, H., R. Smith, and P.R. Sammonds (2008), Evidence for seismogenic fracture of
830 silicic magma, *Nature*, *453*, 511–514.
- 831 Twiss, R.J., and J.R. Unruh (1998), Analysis of fault slip inversions: Do they constrain
832 stress or strain rate?, *J. Geophys. Res.*, *103*, 12205–12222.
- 833 Utsu, T. (1992), On seismicity, *Report of the Joint Res. Inst. for Stat. Math.: Inst. for*
834 *Stat. Math.*, *34*, 139–157.
- 835 Utsu, T. (1999), Representation and analysis of the earthquake size distribution: a his-
836 torical review and some approaches, *Pure Appl. Geophys.*, *155*, 509–535.
- 837 Vavryčůk, V. (2002), Non-double-couple earthquakes of 1997 January in West Bohemia,
838 Czech Republic: evidence of tensile faulting, *Geophys. J. Int.*, *149*, 364–373.
- 839 Vavryčůk, V. (2005), Focal mechanisms in anisotropic media, *Geophys. J. Int.*, *161*, 334–
840 346.
- 841 Vidale, J. (1988), Finite-difference calculation of traveltimes, *Bull. Seismol. Soc. Am.*, *78*,
842 2062–2076.
- 843 Waldhauser, F., and W.L. Ellsworth (2000), A double-difference earthquake location algo-
844 rithm: method and application to the Northern Hayward Fault, California, *Bull. Seism.*

- 845 *Soc. Am.*, 90, 1353–1368.
- 846 Ward, P.L., G. Pálmason, and C. Drake (1969), Microearthquake survey and the Mid-
847 Atlantic Ridge in Iceland, *J. Geophys. Res.*, 74, 665–684.
- 848 Warren, N.W., and G.V. Latham (1970), An experimental study of thermally induced
849 microfracturing and its relation to volcanic seismicity, *J. Geophys. Res.*, 75, 4455–4464.
- 850 Wiemer, S., and S. McNutt (1997), Variations in frequency-magnitude distribution with
851 depth in two volcanic areas: Mount St. Helens, Washington, and Mt. Spurr, Alaska,
852 *Geoph. Res. Letts.*, 24, 189–192.
- 853 Wiemer, S., M. Wyss (2002), Mapping spatial variability of the frequency-magnitude
854 distribution of earthquakes, *Adv. Geophys.*, 45, 259–302.
- 855 Woessner, J., S. Wiemer (2005), Assessing the quality of earthquake catalogues: esti-
856 mating the magnitude of completeness and its uncertainty, *Bull. Seism. Soc. Am.*, 95,
857 684–698.
- 858 Wyss, M. (1973), Towards a physical understanding of the earthquake frequency distri-
859 bution, *Geophys. J. R. astr. Soc.*, 31, 341–359.
- 860 Wyss, M., and J.N. Brune (1968), Seismic moment, stress, and source dimensions for
861 earthquakes in the California-Nevada region, *J. Geophys. Res.*, 73, 4681–4694.
- 862 Wyss, M., B. Liang, W.R. Tanigawa, and X. Wu (1992), Comparison of orientations of
863 stress and strain tensors based on fault plane solutions in Kaoiki, Hawaii, *J. Geophys.*
864 *Res.*, 97, 4769–4790.
- 865 Zierenberg, R.A., et al. (2012), Composition and origin of rhyolite melt intersected by
866 drilling in the Krafla geothermal field, Iceland *Contrib. Mineral. Petrol.*, 165, 327–347.

867 Zoback, M.L., and M. Zoback (1980), State of stress in the conterminous United States,
868 *J. Geophys. Res.*, 85, 6113–6156.

Figure 1. Figure

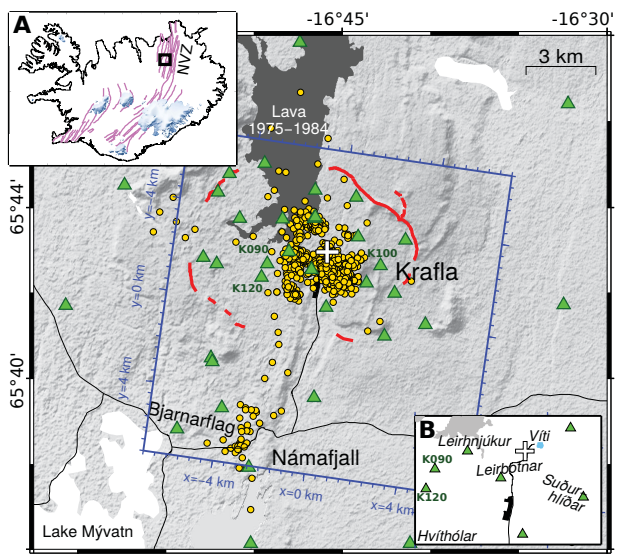


Figure 2. Figure

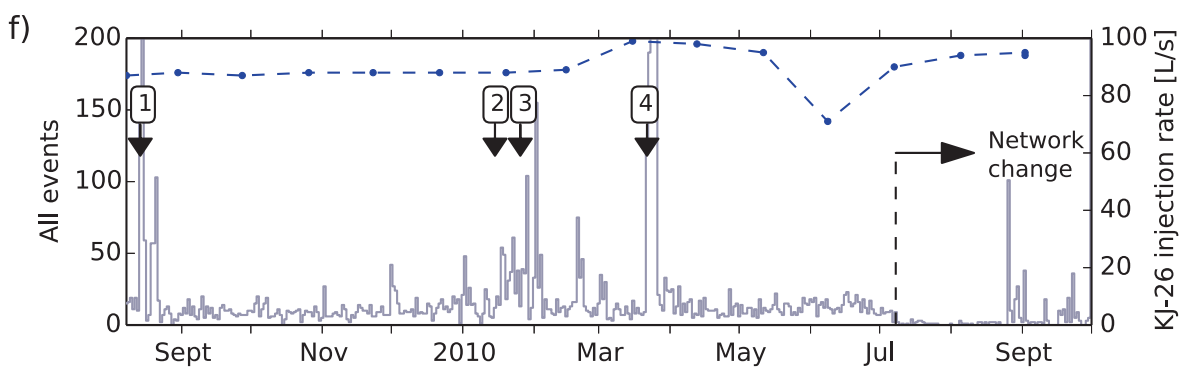
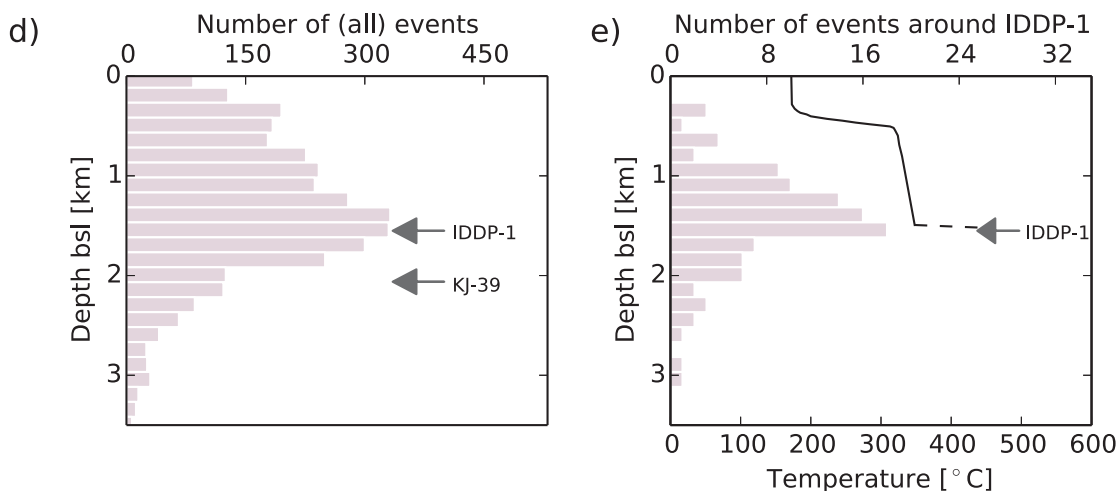
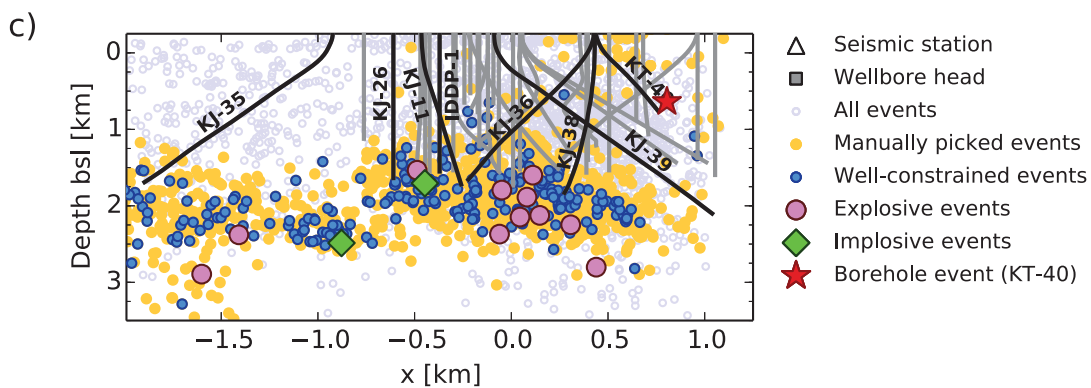
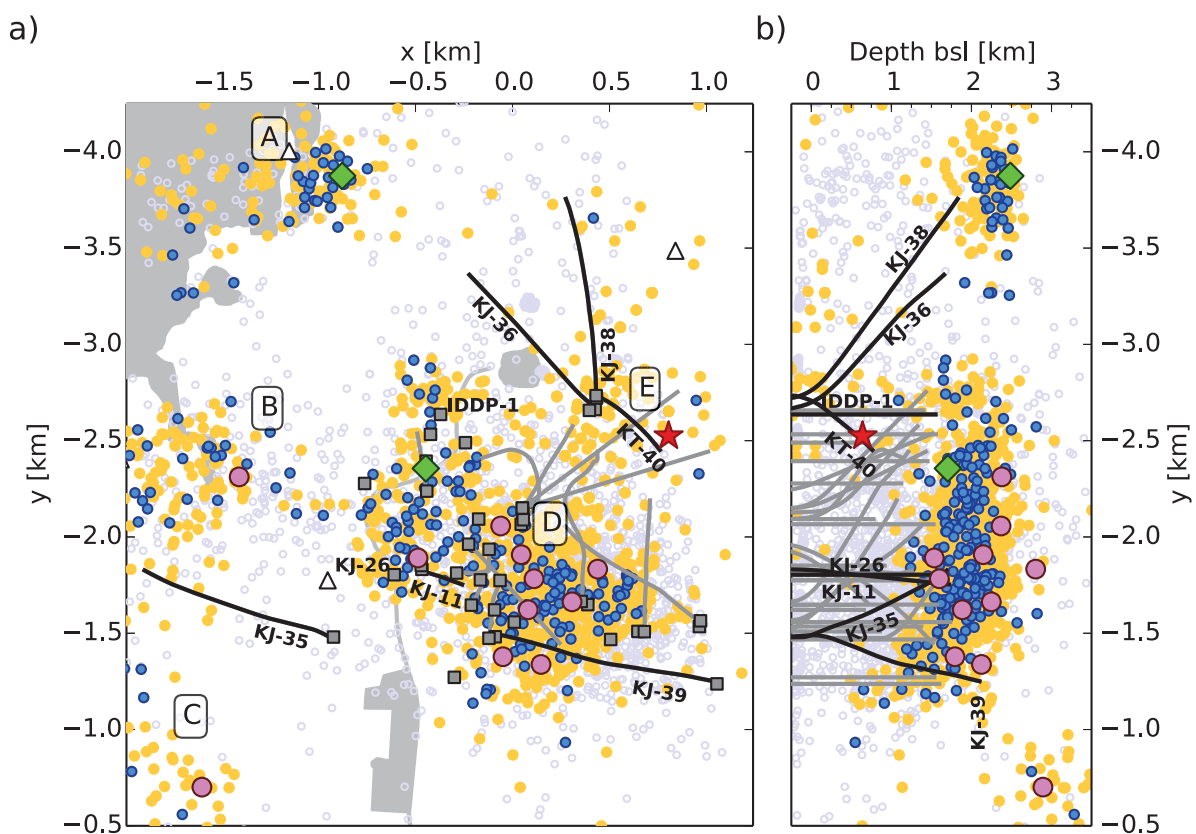
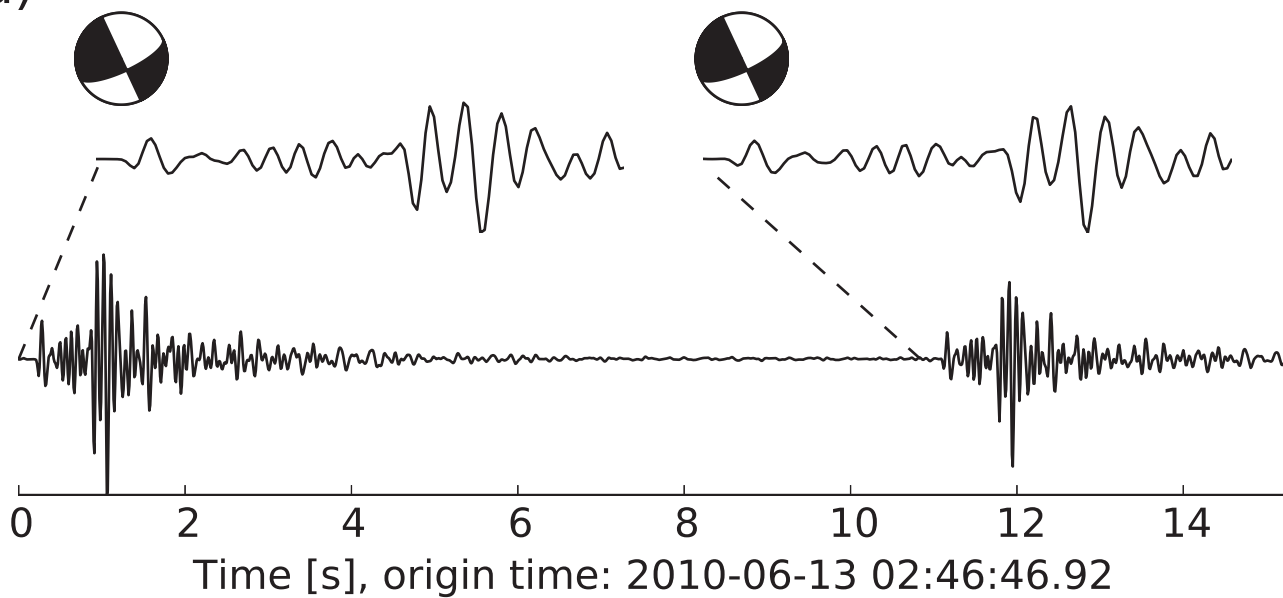


Figure 3. Figure

a)



b)

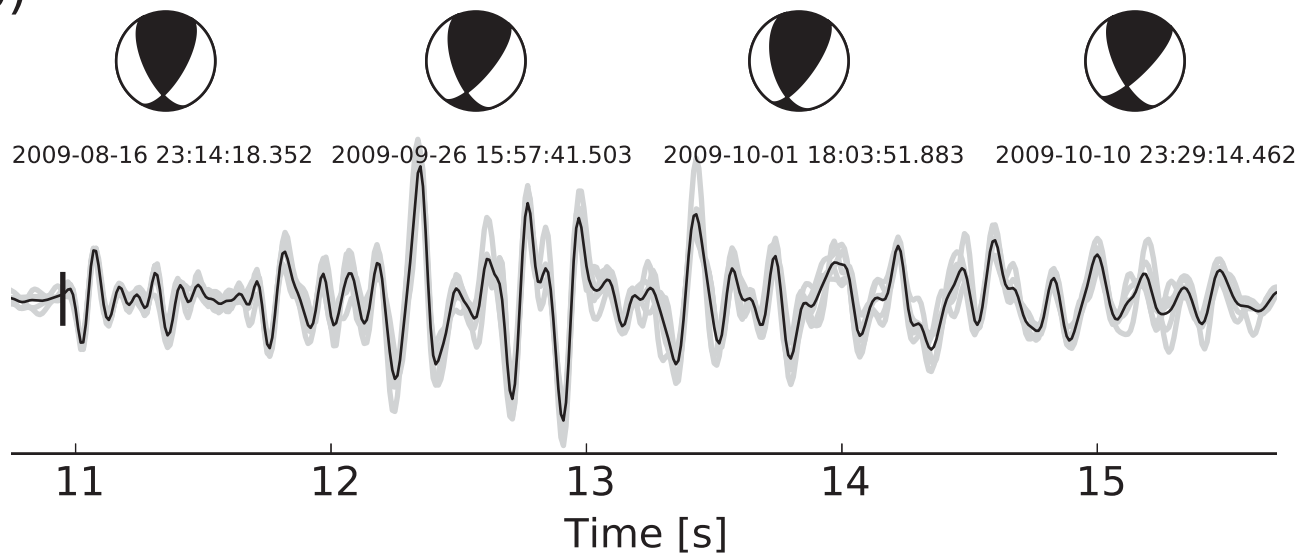


Figure 4. Figure

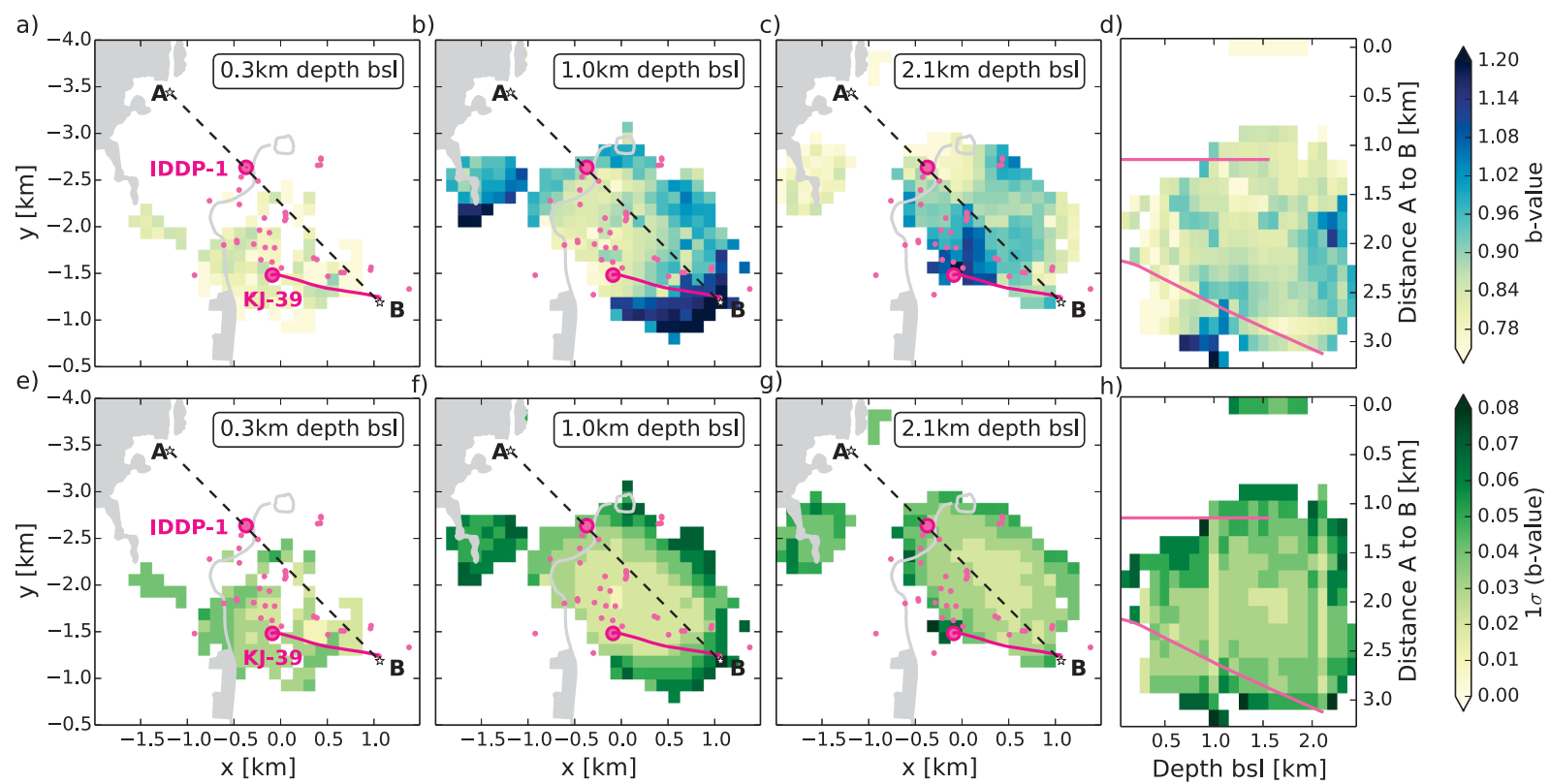


Figure 5. Figure

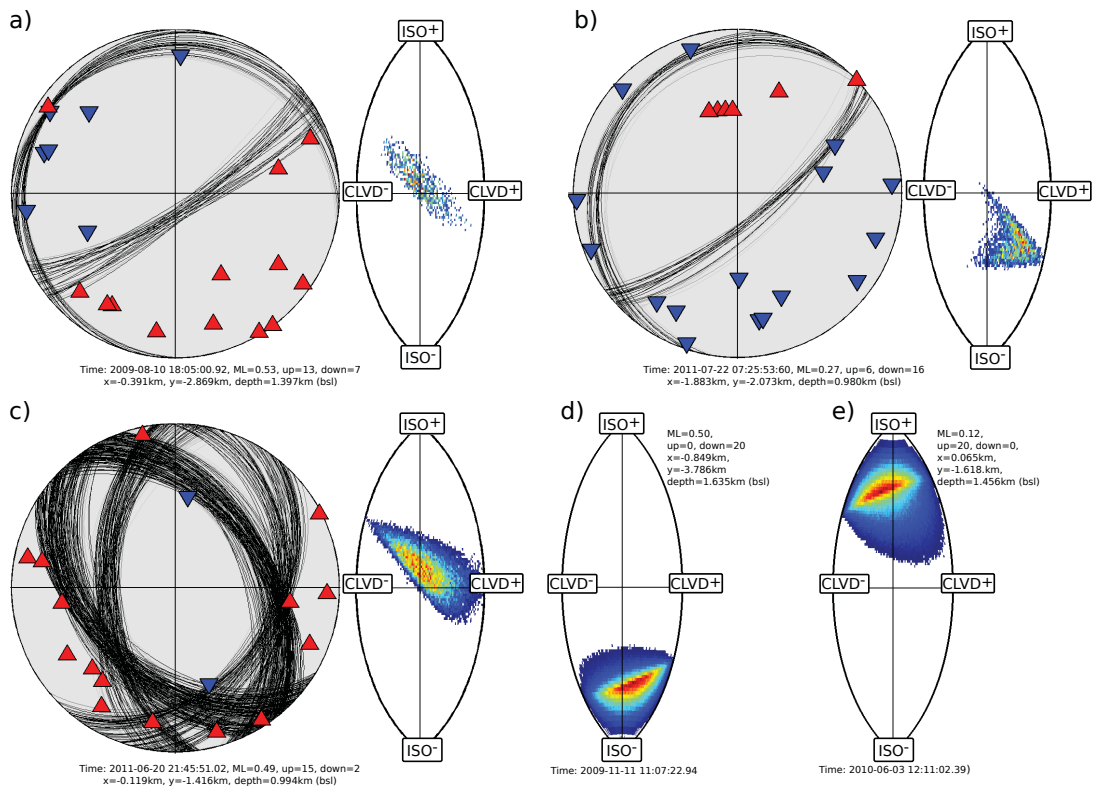


Figure 6. Figure

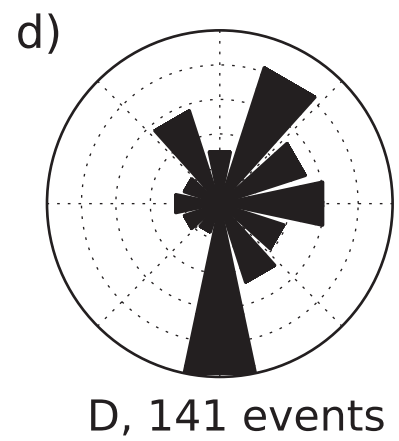
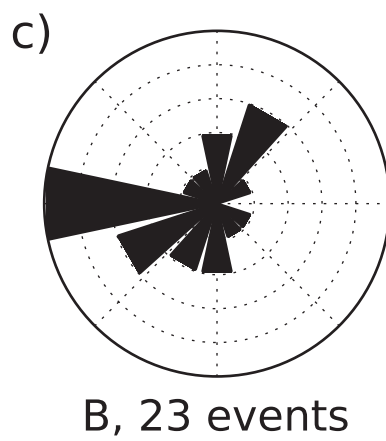
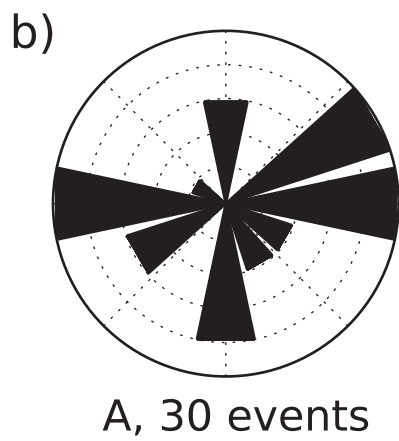
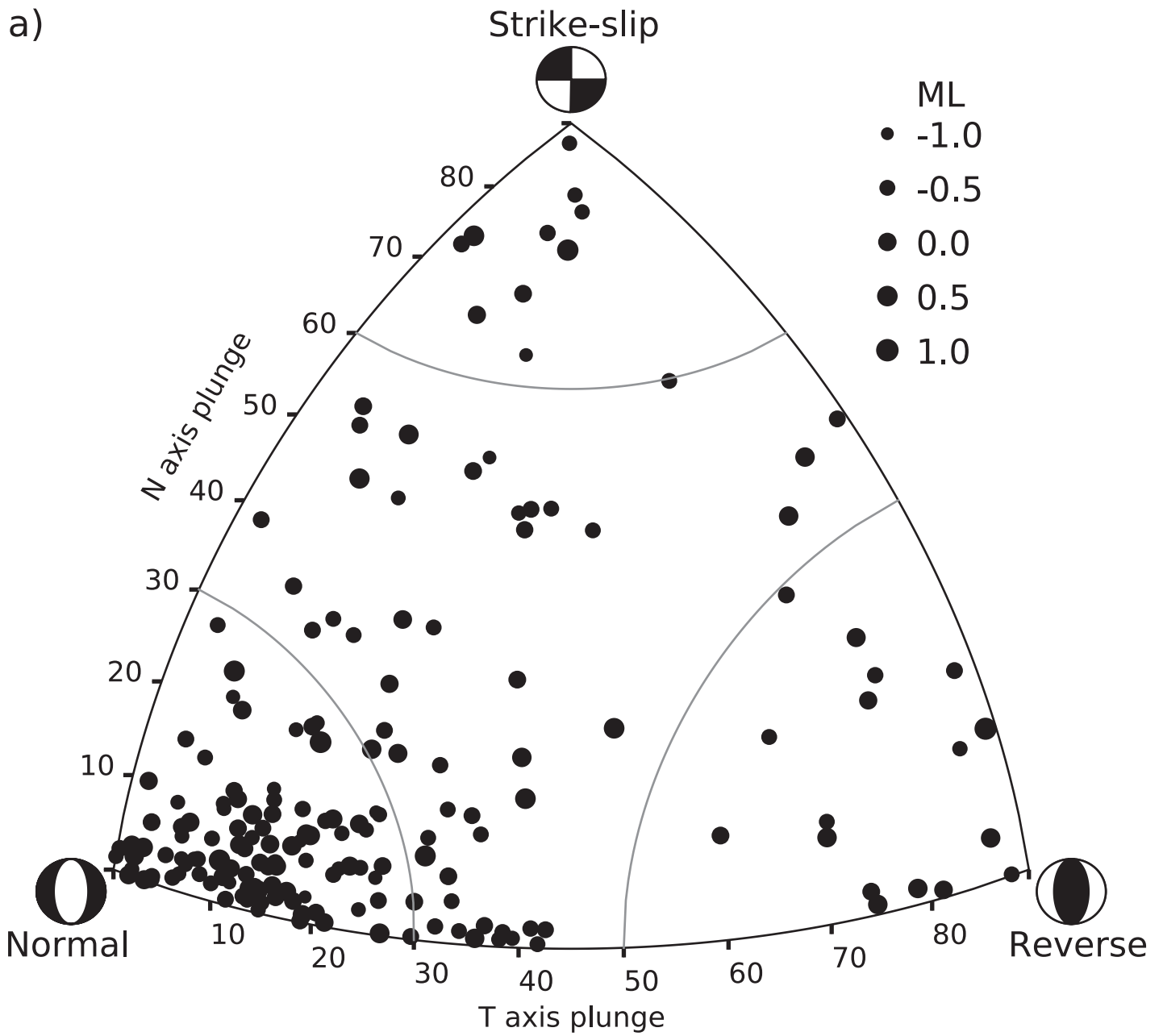


Figure 7. Figure

